Modelling and experimental evaluation of parallel connected lithium ion cells for an electric vehicle battery system

Thomas Bruen[*], James Marco

WMG, University of Warwick, Coventry, CV4 7AL, UK

HIGHLIGHTS

- Experimental evaluation of energy imbalance within parallel connected cells.
- A validated new method of combining equivalent circuit models in parallel.
- Interdependence of capacity, voltage and impedance for calculating cell currents.
- A 30% difference in impedance can result in a 60% difference in peak cell current.
- A difference of over 6% in charge throughput was observed during cycling.

ARTICLE INFO

ABSTRACT

Variations in cell properties are unavoidable and can be caused by manufacturing tolerances and usage conditions. As a result of this, cells connected in series may have different voltages and states of charge that limit the energy and power capability of the complete battery pack. Methods of removing this energy imbalance have been extensively reported within literature. However, there has been little discussion around the effect that such variation has when cells are connected electrically in parallel. This work aims to explore the impact of connecting cells, with varied properties, in parallel and the issues regarding energy imbalance and battery management that may arise. This has been achieved through analysing experimental data and a validated model. The main results from this study highlight that significant differences in current flow can occur between cells within a parallel stack that will affect how the cells age and the temperature distribution within the battery assembly.

1. Introduction

Cells in a battery pack may be electrically connected in parallel in order to increase the pack capacity and meet requirements for power and energy [1,2]. For example, the Tesla Model S 85 kWh battery pack uses 74 3.1 Ah cylindrical cells to create a parallel unit, and 96 of these units in series. Conversely, the Nissan Leaf 24 kWh battery pack consists of 33 Ah cells, with 2 in parallel and 96 in series [3]. The nature of a parallel connection means that the voltage over each cell is the same and the applied current is equal to the sum of the individual cell currents. It is commonly assumed that energy balancing is only required for cells in series [4,5] since the cells in a parallel unit are inherently balanced due to the common

voltage [6,7]. However, there has been little experimental data to explore this further. Variations in internal resistance mean that the cells within a parallel unit will undergo different currents. However, individual cell currents are typically not measured, and so any variation in current is not detected by the battery management system (BMS). Differences in current can change the state of charge (SOC), temperature and degradation rate of each cell [8,9], meaning cells in parallel may not be at the same SOC despite being at the same terminal voltage [10], and could degrade at different rates. State of health (SOH) is often used to quantify cell degradation, with common definitions using the increase in resistance or decrease in capacity relative to when the cell is new [11]. Accurate SOH estimation is a key challenge for battery management systems (BMSs) [12].

The objective of this paper is to introduce a model that allows for thorough analysis of parallel-connected cells in a battery pack, while integrating with existing frameworks. This can be used to aid

* Corresponding author.
  E-mail addresses: thomas.bruen@warwick.ac.uk (T. Bruen), james.marco@warwick.ac.uk (J. Marco).

battery pack design, for example evaluating different series-parallel configurations of cells, and analysis of the temperature distribution within the battery pack. The robustness of BMS functions such as SOC estimation and fault detection can also be tested.

Gogoana et al. [13] cycle-aged two cylindrical lithium iron phosphate (LFP) cells connected in parallel. They found that a 20% difference in internal resistance resulted in a 40% reduction in the useful life of the pair of cells compared to if the cells had approximately equal internal resistances. The authors attribute this to the uneven current distribution between the cells. Their results highlight that each cell will go through periods where it experiences high currents that will in turn age the cells more quickly. Gong et al. [1] drew similar conclusions from their experimental work with 32 Ah cells. When two cells with a 20% impedance difference were connected in parallel, the peak current experienced was 40% higher than if the cells were identical. The authors also performed simulation studies, using the Mathwork's Simscape extension to Simulink to connect two equivalent circuit models (ECMs) in parallel. This is one of the few examples of parallel cell modelling within the literature. Wang et al. also used Simscape for modelling cells in parallel [14], although the current distribution was not analysed in detail. Offer at al. used a simple cell model in Simscape for analysing the effect of poor connection resistance between parallel cells [15]. This effect was explored further in Ref. [10], where an electrochemical model was used to simulate the impact interconnection resistance between cells in parallel has on battery system performance. Often, a parallel unit 'lumped' model is created, where the parameters of a single cell model are scaled to create an effective parallel unit, such as in Ref. [16], in which the authors screen a large batch of cells to ensure that only similar cells are connected in parallel. While this may be valid for new cells, there is no guarantee that the cells will degrade in the same way, as demonstrated in Ref. [17]. Similar assumptions are made in Ref. [6], where the SOC of cells in a parallel is assumed to always be equal. While assumptions such as these allow for the high-level simulation of a battery pack, it assumes the cells within a parallel unit are identical and as such all experience the same electrical and thermal loading. This limits the accuracy of the model and means that some potential physical phenomena, such as temperature gradients and current variations, are not analysed and accounted for as part of a model-based design process. While an acausal approach such as Simscape can account for variations in parameters, it is less well suited to analysis and manipulation than solving a system of ordinary differential equations (ODEs), as is the case for a single cell model.

The contribution of this paper is to extend the existing literature in terms of both simulation method and experimental data. In Section 2 a generic parallel cell model is derived, which allows for the calculation of cell currents and states within a parallel stack while maintaining the same model structure as a single cell model. This means that cells in parallel can be modelled and evaluated within conventional frameworks without having to make assumptions about cell uniformity. The experimental work is introduced in Section 3, in which four commercially available 3 Ah 18650 cells are aged by different amounts to create differences in their respective capacity and impedance. The cells are then connected in parallel and cycle-tested to analyse and quantify the variations in performance, such as current and temperature, which arise from these differences. The model is validated against experimental data in Section 4. Results from the experimental and simulation studies are analysed in Section 5, in which various vehicle usage cases are considered and the impact of using cells in parallel for these applications is evaluated. Conclusions and further work are presented in Section 6.

2. Model development

The ECM is commonly used to simulate the voltage response of individual cells, due to its relative simplicity, ease of parameterisation and real-time feasibility [18,19]. The primary aim of the ECM is to match the voltage response of a physical cell based on a current input, rather than to model the cell using fundamental electrochemical theory. Despite the lack of a physical basis to the model, elements of the circuit can be related to aspects of the cell's physical response, such as charge transfer and diffusion [20].

2.1. Equivalent circuit model

The single cell ECM consists of several elements, as shown in Fig. 1a: the open circuit voltage v_{OC}, internal resistance R_D and a resistor-capacitor (RC) pair, which is a resistor R_p and capacitor C_p in parallel. Multiple RC pairs in series can be used depending on the bandwidth and fidelity of the response required. Eq. (1) shows that for a given current i_{cell}, the terminal voltage v_t is comprised of the v_{OC}, the voltage over the internal resistance and the sum of the RC pair voltages v_p. v_p and SOC are governed by ODEs, given by (2) and (3) respectively. Typically, v_{OC} is not calculated directly; instead SOC is calculated using (3), where Q is the cell capacity in Ah, and v_{OC} found from (4). Unlike (3), the v_{OC}-SOC function in (4) is typically nonlinear. By treating SOC, not v_{OC}, as a model state variable, the state equations are kept linear. Commonly, systems such as this are written in state-space form as in (5). The system for one RC pair is shown in linear state-space form in (6). Throughout this paper, a one-to-one relationship between SOC and v_{OC} has been assumed, which can often be considered sufficiently accurate [21]. In reality the cell response may exhibit hysteresis, in which the v_{OC} at a given SOC may be different depending on whether the cell is being charged or discharged. As discussed in Ref. [22], this can be accounted for by adding additional states (ODEs) to the model.

$$v_t = v_{OC} + R_D i_{cell} + \sum_{n=1}^{N} v_{p,n} \tag{1}$$

$$\dot{v}_p = -\frac{v_p}{R_p C_p} + \frac{i_{cell}}{C_p} \tag{2}$$

$$\dot{SOC} = \frac{i_{cell}}{36Q} \tag{3}$$

$$v_{oc} = f(SOC) \tag{4}$$

$$\dot{x} = Ax + Bu \\ y = Cx + Du \tag{5}$$

$$\begin{bmatrix} \dot{SOC} \\ \dot{v}_p \end{bmatrix} = \begin{bmatrix} 0 & 0 \\ 0 & -\frac{1}{R_p C_p} \end{bmatrix} \begin{bmatrix} SOC \\ v_p \end{bmatrix} + \begin{bmatrix} \frac{1}{36Q} \\ \frac{1}{C_p} \end{bmatrix} i_{cell} \tag{6}$$

$$\begin{bmatrix} v_t \end{bmatrix} = \begin{bmatrix} \frac{f(SOC)}{SOC} & 1 \end{bmatrix} \begin{bmatrix} SOC \\ v_p \end{bmatrix} + \begin{bmatrix} R_D \end{bmatrix} i_{cell}$$
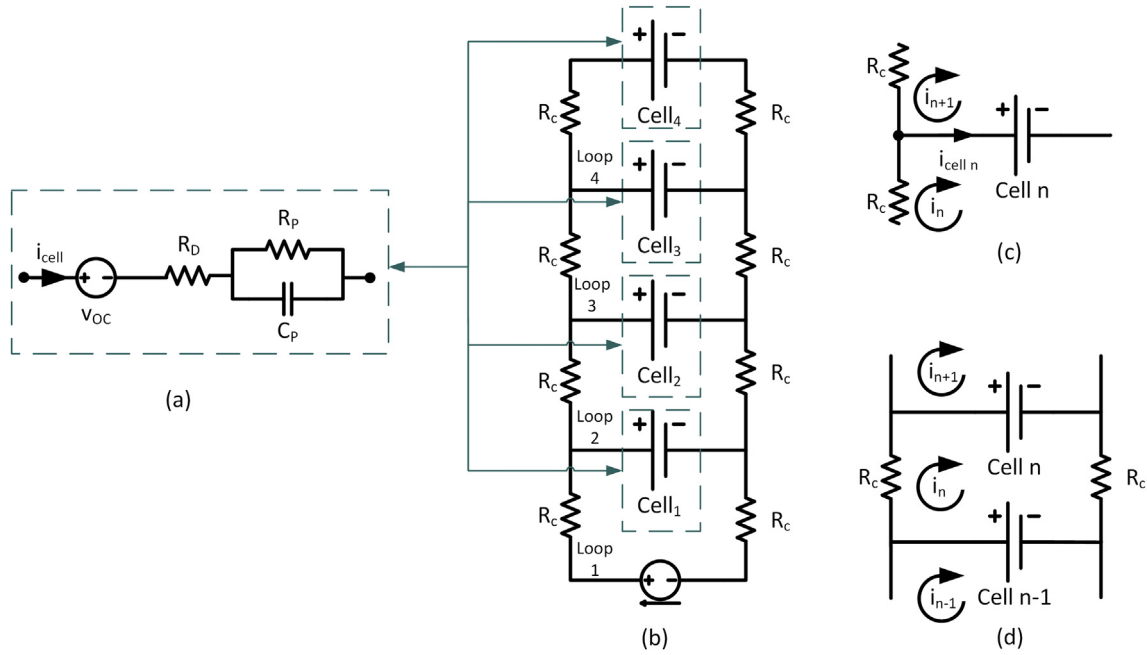
Fig. 1. (a) Equivalent Circuit Model; (b) Schematic of four cells connected in parallel; (c) Mesh junction for cell n; (d) Mesh Loop for cell n.

2.2. Parallel equivalent circuit model

The ECM in Section 2.1 can be expanded to incorporate any number of cells in parallel. For this derivation, four cells with one RC pair each is used, but the methodology is generic and can be extended to any number of cells or RC pairs. Fig. 1b presents a schematic of four cells in parallel with an interconnection resistance (R_c) between each terminal. Each cell is represented by its own ECM as in Fig. 1a.

In addition to the state equations for the single cell, there are also algebraic constraints on the parallel cell system. These are based on Kirchoff's laws for current and voltage. The currents at a junction must sum to zero, which for the parallel cell system occurs at the cell connections, as shown Fig. 1c. For N cells, Eq. (7) describes the relationship between loop currents i_1 to i_N and cell currents $i_{cell\ 1}$ to $i_{cell\ N}$. The two cases arise due to there being no i_{n+1} for the final cell.

$$i_{cell\ n} = \begin{cases} i_n - i_{n+1}, & n < N \\ i_n, & n \equiv N \end{cases} \quad (7)$$

Similarly, the voltages around a loop must sum to zero. A typical loop for cell n is shown in Fig. 1d. There are N-1 loops to solve, as the first loop current is the current source and is therefore trivial. The voltage loop equation is given by (8), and can be expanded to (9) by defining the cell voltage through its constituent components according to (1).

$$v_{t\ n} - v_{t\ n-1} + 2R_c i_n = 0 \quad (8)$$

In order to work with the algebraic equations in (9) it is convenient to use v_{OC} as a state rather than *SOC*. This moves the nonlinear function from the output matrix *C* to the input matrix *B*, but does not affect the state matrix *A* and so the system poles remain unchanged. To achieve this, an effective capacitance, C_0 is defined, which determines how much charge is required to cause a given change in v_{OC}. As it can be seen in (10), C_0 is found by calculating the gradient of the v_{OC}-*SOC* curve and factoring in cell capacity *Q* in Ah. The resulting state equation is given by (11). This equation is still an integrator like Eq. (3), and there is no change in the overall transfer function of the system. The cell equations now take the form of (12).

$$C_0(v_{OC}) = 36Q \frac{dSOC(v_{OC})}{dv_{OC}} \quad (10)$$

$$\dot{v_{OC}} = \frac{i_{cell}}{C_0} \quad (11)$$

$$\begin{bmatrix} \dot{v_{OC}} \\ \dot{v_p} \end{bmatrix} = \begin{bmatrix} 0 & 0 \\ 0 & -\dfrac{1}{R_p C_p} \end{bmatrix} \begin{bmatrix} v_{OC} \\ v_p \end{bmatrix} + \begin{bmatrix} \dfrac{1}{C_0} \\ \dfrac{1}{C_p} \end{bmatrix} i_{cell}$$

$$\begin{bmatrix} v_t \end{bmatrix} = \begin{bmatrix} 1 & 1 \end{bmatrix} \begin{bmatrix} v_{OC} \\ v_p \end{bmatrix} + \begin{bmatrix} R_D \end{bmatrix} i_{cell} \quad (12)$$

Fig. 2a shows v_{OC} as a function of *SOC* for the cell type employed for this research. Fig. 2b then shows how this is translated into a

$$0 = \begin{cases} v_{OC\ n} - v_{OC\ n-1} + v_{p\ n} - v_{p\ n-1} + R_{D\ n}(i_n - i_{n+1}) - R_{D\ n-1}(i_{n-1} - i_n) + 2R_c i_n, & n < N \\ v_{OC\ n} - v_{OC\ n-1} + v_{p\ n} - v_{p\ n-1} + R_{D\ n} i_n - R_{D\ n-1}(i_{n-1} - i_n) + 2R_c i_n, & n \equiv N \end{cases} \quad (9)$$
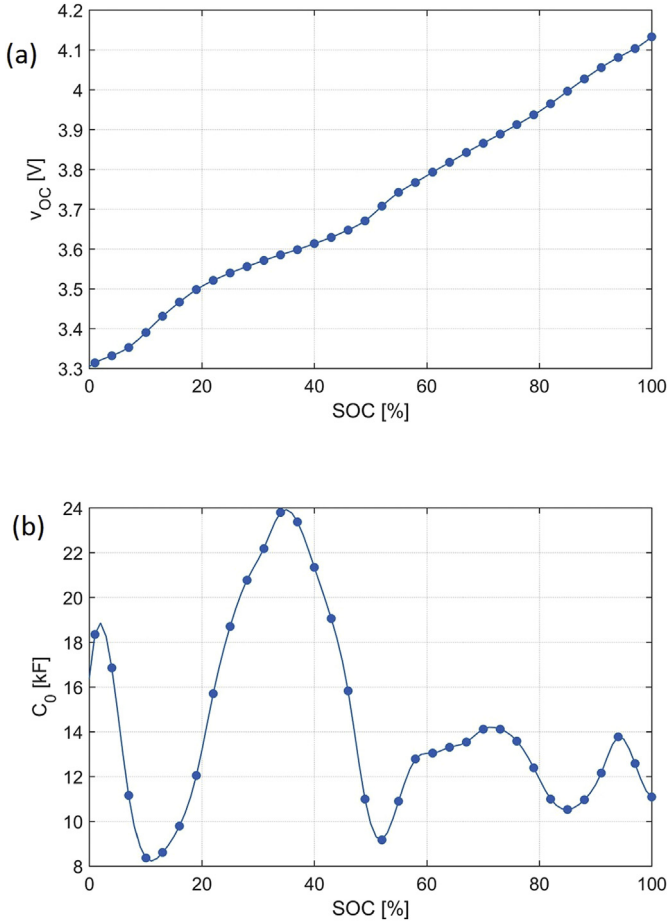
Fig. 2. (a): v_{OC} as a function of SOC for the cell under test; (b) Effective capacitance (C_0) as a function of SOC.

C_0–SOC curve through applying (10). It can be seen that a larger C_0 value corresponds to a flatter gradient at that point of the v_{OC}-SOC curve, since in this region more charge is required to create a given change in v_{OC}. The C_0 curve is less smooth than the v_{OC} curve and care must be taken in terms of data acquisition and interpolation method to ensure the gradient remains accurate. This is particularly the case for LFP cells, where v_{OC}-SOC curve is known to have a flat region, which will result in a large value of C_0 [23].

The individual cell state equations in (12) can be merged to form one larger solution as in (13) by creating block diagonals of each matrix and concatenating the state and input vectors. Despite there now being N cells and N inputs, the output (v_t) is the same for all cells and so the output equation for any single cell can be applied rather than calculating all of them. In this case the output equation for the first cell has been applied.

$$\begin{bmatrix} \dot{x}_1 \\ \dot{x}_2 \\ \vdots \\ \dot{x}_N \end{bmatrix} = \begin{bmatrix} A_1 & & & \\ & A_2 & & \\ & & \ddots & \\ & & & A_N \end{bmatrix} \begin{bmatrix} x_1 \\ x_2 \\ \vdots \\ x_N \end{bmatrix} + \begin{bmatrix} B_1 & & & \\ & B_2 & & \\ & & \ddots & \\ & & & B_N \end{bmatrix} \begin{bmatrix} i_{cell,\,1} \\ i_{cell,\,2} \\ \vdots \\ i_{cell,\,N} \end{bmatrix}$$

$$[v_t] = [C_1 \ \ 0 \ \ 0 \ \ \dots \ \ 0] \begin{bmatrix} x_1 \\ x_2 \\ \vdots \\ x_N \end{bmatrix} + [D_1 \ \ 0 \ \ 0 \ \ \dots \ \ 0] \begin{bmatrix} i_{cell,\,1} \\ i_{cell,\,2} \\ \vdots \\ i_{cell,\,N} \end{bmatrix} \tag{13}$$

By analysing the structure and resulting Eigenvalues of the

system state matrix of (13) it can be seen that the dynamics of each cell remain independent, and an input vector of cell currents is required. However, cell currents are typically not measured and so instead the system input needs to be the scalar measured current i_1. This is achieved by writing the voltage loop algebraic Eq. (9) in matrix form as in (14). This introduces three matrices: the resistance matrix R, which is a tridiagonal square matrix of cell and interconnection resistances, the state dependency matrix E, which uses the state vector to create the voltage differences and the input dependency vector F to account for i_1.

$$R \begin{bmatrix} i_1 \\ i_2 \\ \vdots \\ i_N \end{bmatrix} = Ex + Fi_1$$

$$R = \begin{bmatrix} 1 & 0 & 0 & 0 \\ 0 & -(R_{D,1}+R_{D,2}+2R_c) & R_{D,2} & 0 \\ 0 & R_{D,2} & \ddots & R_{D,N-1} \\ 0 & 0 & R_{D,N-1} & -(R_{D,N-1}+R_{D,N}+2R_c) \end{bmatrix}$$

$$E \begin{bmatrix} 0 & 0 & \dots & & & \dots & 0 \\ -1 & -1 & 1 & 1 & 0 & \dots & 0 \\ 0 & \dots & -1 & -1 & 1 & 1 & 0 & 0 \\ 0 & \dots & & 0 & -1 & -1 & 1 & 1 \end{bmatrix}$$

$$F = \begin{bmatrix} 1 \\ -(R_{D,1}+2R_c) \\ 0 \\ \vdots \\ 0 \end{bmatrix} \tag{14}$$

By inverting R, a vector of loop currents can be solved for. Eq. (15) introduces the current translation matrix G, to calculate the individual cell currents from the loop currents in (14), i.e. applying (7) in matrix form. This shows that the cell currents can be written as a function of the cells' states and the input current.

$$\begin{bmatrix} i_{cell\,1} \\ i_{cell\,2} \\ \vdots \\ i_{cell\,N} \end{bmatrix} = GR^{-1}(Ex + Fi_1)$$

$$G = \begin{bmatrix} 1 & -1 & 0 & 0 \\ 0 & 1 & -1 & 0 \\ 0 & \ddots & 1 & -1 \\ 0 & \dots & 0 & 1 \end{bmatrix} \tag{15}$$

The cell current vector in (15) is also the input vector for (13) and so can be substituted to create (16). For convenience, the solution can be grouped into state and input components to give the augmented state-space solution in (17). These equations demonstrate that the states of all cells in parallel can be written using the same inputs and outputs as for a single cell. This facilitates the use of established control theory methods and also enables a more thorough analysis of the individual and collective response of cells when connected in parallel.

$$\begin{aligned} \dot{x} &= Ax + B\big[GR^{-1}(Ex + Fi_1)\big] \\ y &= Cx + D\big[GR^{-1}(Ex + Fi_1)\big] \end{aligned} \tag{16}$$

$$\begin{aligned} \dot{x} &= A'x + B'i_1 \\ y &= C'x + D'i_1 \\ A' &= A + BGR^{-1}E \\ B' &= BGR^{-1}F \\ C' &= C + DGR^{-1}E \\ D' &= DGR^{-1}F \end{aligned} \tag{17}$$

Established control theory states that the system poles for a

state-space model can be found using (18). For individual cells, an analytical solution to the eigenvalues is straightforward as the A matrix is a leading diagonal matrix; the solution is given in (19). However, for the parallel system the A' matrix is full and finding the eigenvalues analytically is complicated even for a simple case.

$$p = eig\left(A'\right) \tag{18}$$

$$p = \left[0 \, , \, -\frac{1}{R_p C_p}\right] \tag{19}$$

Whereas for a single cell model the system pole for V_{OC} (or SOC) is zero, this is no longer the case for the cells in parallel. The self-balancing interactions imply a slow, stable convergence and as such the system contains negative poles to account for this. The self-balancing poles for the parallel system can be approximated by (20). For the cells used for this work, the time constant for the self-balancing dynamics was in the region of 500–600 s, depending on factors such as impedance and SOC.

$$p \approx \frac{-1}{C_0\left(R_D + \sum_{n=1}^{nRC} R_{p,n}\right)} \tag{20}$$

3. Experimental procedure

The new modelling framework derived in Section 2.2 requires parameterisation and validation against experimental data to fully explore its accuracy and robustness. Additionally, data from physical cell testing will also help to determine the appropriate bandwidth of the model, to ensure that the cells' responses, and any interactions, are reliably captured. For the following experimental work, four 3Ah 18650 lithium ion cells were used. The specifics of the data acquisition required for parallel cell measurement is detailed in Section 3.1.

3.1. Cell current measurement

A Bitrode MCV16-100-5 was used to control the applied current. However, this equipment cannot measure current through cells in parallel as only the total circuit current applied to the parallel unit is measured. A measure of the unique cell currents is required for analysis purposes as well as to validate the model. To measure the current through each cell, a 10 mΩ shunt resistor with less than 500 ppm K^{-1} thermal sensitivity was connected in series with each cell. This has the disadvantage of changing the resistance of each string, meaning the absolute value of current through each cell is different than if the shunt resistors were not in the circuit. Hall-effect sensors can be used to sense current without being a part of the circuit and so do not impact the result. However, the accuracy and resolution were considered insufficient for this test, especially for capturing the low magnitude self-balancing currents.

The voltage over each resistor is proportional to the current. Each resistor was calibrated by passing a number of known currents through the resistor and measuring the voltage over the resistor. The current–voltage relationship was obtained through a least

squares solution. The calibration can be verified once the cells are connected in parallel. In this case the sum of each cell current, found using the shunt voltage, should sum to the applied current measured by the cell cycler. Another current profile was run with the cells connected in parallel, and the sum of the measured shunt currents was compared to the measured applied current. The results, given in Table 1, show that the total current estimated from the shunt voltage is less than 0.1% different to the applied current.

3.2. Cell testing

The procedure for the cell testing can be divided into two distinct phases. Characterisation testing is used to obtain the cells' capacity and impedance and so calculate the ECM parameters required to allow the model derived in Section 2.2 to be executed in simulation. The cycle ageing test is used to cause capacity fade and impedance rise in the cells. By ageing each of the four cells by different amounts, a noticeably different impedance and capacity is generated for each cell, ensuring that there will be significant differences in cell current, when connected in parallel, under load. The characterisation was performed twice: once when the cells were new and once after they had been aged. To reduce uncertainty within the experimental results, all of the tests were performed at 25 °C. For all of these tests, the cells were controlled individually, not connected in parallel.

3.2.1. Cell characterisation

Cell characterisation consists of four tests: capacity measurement, defining the v_{OC}-SOC relationship, and impedance measurement through both pulse power tests and the use of electrochemical impedance spectroscopy (EIS).

1. Capacity: to measure the capacity, each cell was subject to C/3 constant-current 4.2 V constant-voltage charging according to the manufacturer's specification to close to 100% SOC, where it is allowed to rest for 3 h. It was then discharged at 1C until the manufacturer defined lower voltage limit of 2.5 V was reached. The charge accumulated up to this point is taken to be the cell's capacity.
2. A pseudo-v_{OC}-SOC curve was obtained by discharging each cell at C/25 and normalising the results against the 1C capacity measurement. The C/25 current is low enough that the effect of impedance is considered negligible and the terminal voltage is approximately equal to v_{OC}.
3. Pulse power tests: the data from this test is used to fit an ECM to each cell. Each pulse consists of a 10 s current followed by a 30 min rest, allowing the cell to settle such that the measured cell voltage is approximately equal to v_{OC}. In a pulse test there are ten pulses: five charging, five discharging, at increasing magnitudes and scaled relative to the maximum current rate of the cell. The pulse test is repeated at 20%, 50%, 80% and 95% SOC to capture the impedance variation across the SOC range. Results from an example pulse test at 50% SOC are shown in Fig. 3, with a zoomed-in plot for the third charging pulse to show the typical response of the cell.
4. EIS: The EIS test was performed with a peak current amplitude of C/20, from 100 kHz down to 10 mHz. The high frequency

Table 1
Comparison of applied and measured current.

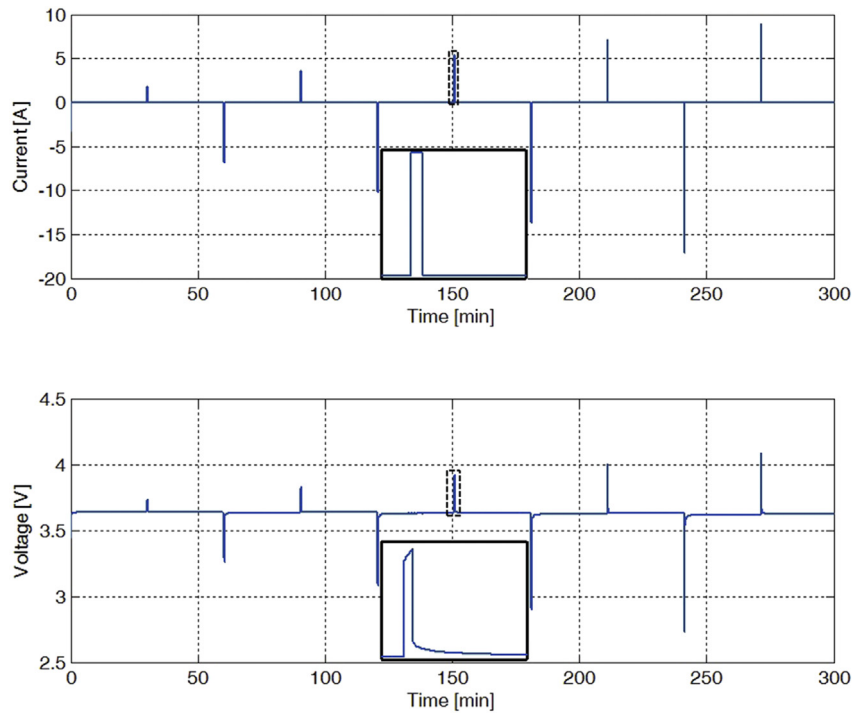| Applied current (A)	6	12	24	0	−24	−12	−6
Estimated net current (A)	5.9981	11.998	24.011	0.00042	−24.005	−12.007	−6.0053
Error (%)	−0.03	−0.02	0.05	–	0.02	0.06	0.09

Fig. 3. Current and voltage measurements for a pulse test at 50% SOC.
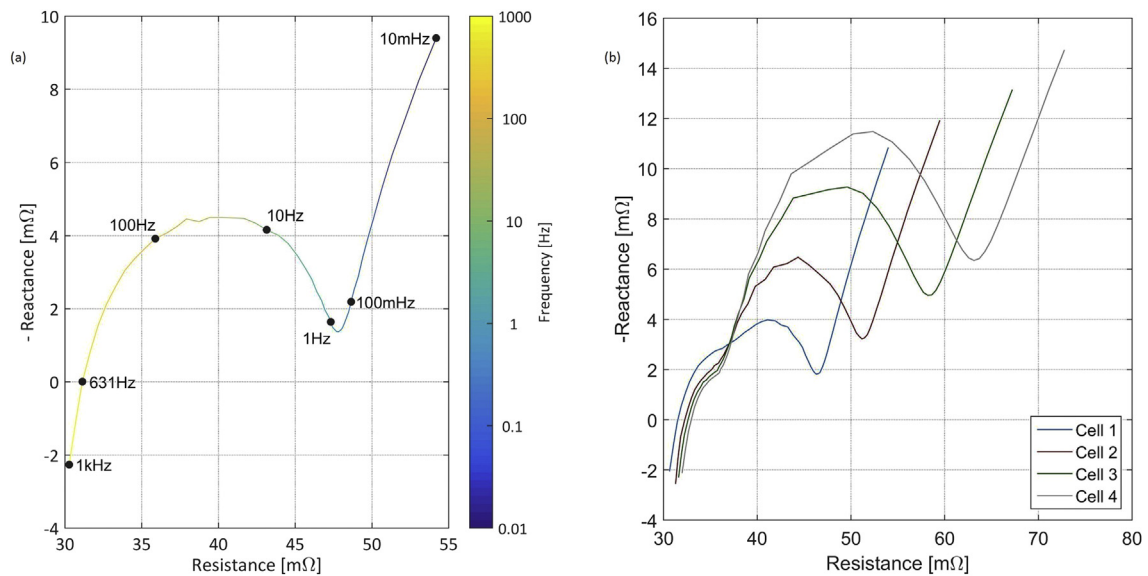

Fig. 4. (a): Nyquist plot for one new cell at 50% SOC (b) Nyquist plot of the four aged cells, at 50% SOC.

inductive region was ignored since inductance is not accounted for in the model. An example Nyquist plot of impedance for a new cell at 50% SOC is given in Fig. 4a, with various frequencies annotated for clarity. Typically, the high frequency region (10—1000 Hz) is most affected by ageing [24], which means the lower frequency region of the impedance curve on the Nyquist plot will shift to the right. This can be seen in the ageing results in Fig. 4b, discussed in Section 3.2.2. The lowest frequency region of the impedance curve corresponds to diffusion in the electrodes [25]. This region goes up to the turning point in the curve − just under 1 Hz in the figure and the impedance at this point is used as a metric to quantify cell ageing.

3.2.2. Cycle ageing

Each ageing cycle consists of a 1C (3 A) discharge to 2.5 V followed by a constant current-constant voltage charge at C/2 (1.5 A) to 4.2 V. The cycle was chosen to age the cells quickly without overstressing the cells; the current magnitude is not at the cell's limit, but the full Depth of Discharge (DOD) ages the cells faster than a narrow DOD cycle [26]. The four cells were each aged by different amounts in order to ensure that each cell would have significantly different impedance and capacity values. The cells were aged by 0, 50, 100 and 150 cycles respectively. The two main metrics of cell ageing are impedance rise and capacity fade [8]. The results in Table 2 show that the ageing cycles cause a steady

Table 2
Summary of cell ageing results.

Cell	Ageing cycles	1C discharge capacity (Ah)	Turning point resistance (mΩ)
Nominal	–	3.07	48.1
1	0	2.94	46.3
2	50	2.86	51.2
3	100	2.77	58.2
4	150	2.65	63.1

increase in resistance and decrease in capacity. The change in impedance for the cells at 50% SOC can be seen in Fig. 4b. There is some increase in ohmic resistance with age, but the largest change in impedance occurs because of the growth of the semicircle at around 20 Hz. This pushes the low frequency diffusive region of the curve to the right, increasing the effective resistance of the cells as they age.

4. Model parameterisation and validation

The pulse power test data described in Section 3.2.1 were used to identify model parameters for each cell. A nonlinear least squares algorithm was used to estimate the vector of unknown model parameters Θ. aording to (21). This cost function aims to minimise the difference in voltage between the measured voltage v_t. d the estimated voltage $\widehat{v}_t$.

$$\underset{\Theta}{\operatorname{argmin}} \sum_{n=1}^{N} [v_{t_n} \widehat{v}_{t_n}(t, i_{cell}, \Theta)]^2$$

$$\Theta = [R_D, R_{P,1}, C_{P,1} \dots C_{P,nRC}]$$

$$(21)$$

A real-world test profile derived from an EV operating in an urban environment was employed to exercise the four cells connected in parallel and to check the accuracy of the parameterisation. The peak current was 4C and the root mean square (RMS) current was 1.8 C. The test was initialised at 70% SOC. A 6.5% reduction in SOC over the 20 min duration of the test was observed. Fig. 5 shows the applied current for the test profile. This profile was also employed as an input to the parameterised parallel cell model. The cell currents calculated using the model were compared with the cell currents measured during the test to quantify the accuracy of the parallel cell model.
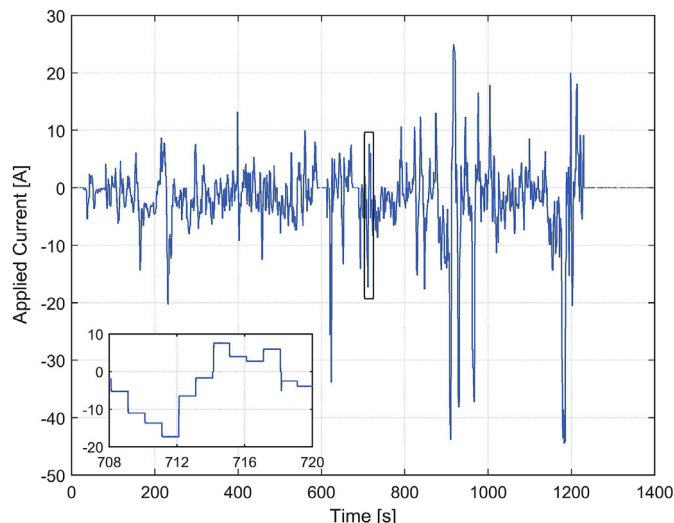

Fig. 5. Current profile for validation drive cycle.

The individual ECMs were initially parameterised using data sampled at 10 Hz, the maximum rate of the cell cycler. However, the cell currents were logged using a separate data logger sampling at 100 Hz. When the parameters obtained from 10 Hz data were used for model validation, the current distribution was found to be relatively inaccurate. This is because after each change in applied current, the cell current distribution is initially dominated by the high frequency impedance of the cell. The sampling rate for pulse power tests will typically not be high enough to capture the true DC resistance and instead the ohmic resistance (R_D) will be the resistive component of the impedance beyond the sampling frequency [27]. From Fig. 4 it can be seen that the actual DC resistance, which occurs at 631 Hz, will be much better approximated by R_D when captured with 100 Hz data than with 10 Hz data. This means the RC pairs are fitted across the frequency spectrum and better capture the high frequency response of the cell, which improves the accuracy of the cell current calculation.

Table 3 shows a comparison of the peak and RMS error in cell current and terminal voltage for five model parameterisations. 1–3 RC pairs are fitted to the 100 Hz data, and 1–2 RC pairs are fitted to the 10 Hz data (only the 100 Hz data is parameterised with a third RC pair because of its wider bandwidth). The 2RC model using the 10 Hz data has similar accuracy to the 1RC model using the 100 Hz data, because the time constants of the models parameterised at 100 Hz are generally faster than those from the 10 Hz models. This shows that the sampling rate is important as well as model order. For current, the RMS and peak error both decrease as the number of RC pairs increases. The 3RC model, which contains the fastest time constant, is accurate to 2%, based on the RMS of the applied current. There is a similar trend with terminal voltage. A snapshot of the experimental and simulated current using 3RC pairs for the four cells is shown in Fig. 6, including a zoomed-in region covering 2 s. It can be seen that for all four cells, the simulated current (solid lines) matches the measured current (dashed lines) well, even when the current distribution is changed significantly due to a step change in the applied current.

These results show that some of the most important aspects of a parallel cell unit's response occurs at high frequencies. This can be the region in which the greatest divergence in current occurs. However, a typical BMS sampling rate of 1 Hz would not capture this response, even if there were current sensors for the parallel branches. A model could estimate the current, but it would not be possible to re-parameterise the fastest RC pair components online as the cell ages.

Table 3
Comparison of error between simulated and experimental data for various models.

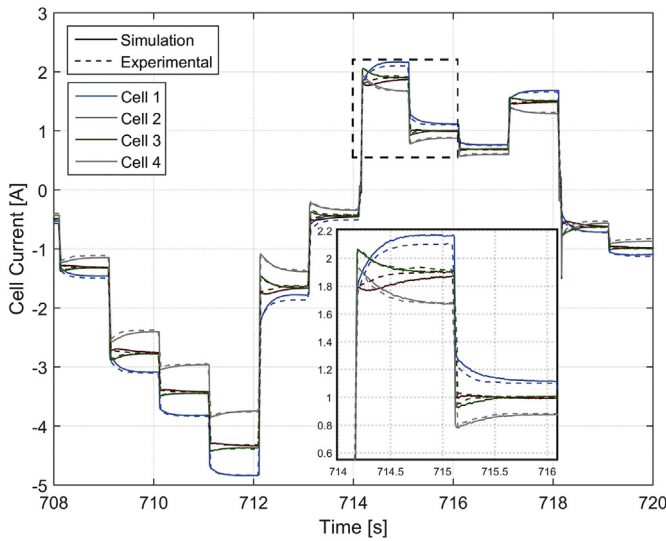| Sample rate	100 Hz			10 Hz	
RC Pairs	1	2	3	1	2
RMS Error– Current (mA)	60.94	51.62	36.94	63.65	60.36
Peak Error– Current (mA)	522.2	510.1	358.9	743.6	493.2
RMS Error– Voltage (mV)	16.24	14.30	8.87	29.32	29.85
Peak Error– Voltage (mV)	92.76	88.4	79.1	185.7	194.5

Fig. 6. Comparison of simulated and experimental currents for the validation test profile.

5. Analysis

Two main applications for electric vehicles are considered. Firstly, a hybrid electric vehicle (HEV) type drive cycle, where the overall change in SOC is low but the current profile is very dynamic and relatively large current magnitudes are expected. Secondly, a battery electric vehicle (BEV) drive cycle, in which the currents are lower but the SOC window of operation is much wider. Additionally, the effects of interconnection resistance and cell disconnection - two factors unique to cells connected in parallel are explored further using the validated modelling framework.

5.1. HEV application

The same current profile as the validation current (shown in Fig. 5) was used to assess HEV applications. This was employed as the input to the parallel cell model, but with the shunt resistors removed to simulate the cells as they would be in a conventional battery pack. Two metrics are used to evaluate the cell current over the drive cycle: the peak current, and the overall charge throughput, given by (22). The peak current is scaled relative to what it would be if all cells were identical, i.e. the applied current at that time divided by the number of cells. Similarly, the charge throughput would be 25% for all of the cells if they were identical. These results are shown in Table 4. As it can be seen, cell 1 experiences 7% more charge throughput than cell 4, which as discussed in Ref. [8] would lead to faster ageing and higher localised temperatures within the system. Additionally, the SOC of cell was 4 consistently higher than the others, implying that for a HEV type application the increase in cell resistance has a greater detrimental impact than the corresponding reduction in decrease in cell capacity.

$$q_{norm} = 100 \frac{\int |i_{cell}|}{\int |i_{app}|} \qquad (22)$$

It was observed that following a step change in current, in some instances the cell currents diverge and at other times they converge. This effect has to do with the magnitude of applied current. If the applied current is low, the self-balancing nature of the cells dominates the system response. The relative difference in cell current will decrease as the cells reach the same SOC. However, this is actually at odds with the dynamics of a parallel cell system. As Fig. 4b shows, all of the aged cells have a similar high-frequency resistance with a larger difference at lower frequencies. As such, for a very short time period (in the millisecond range) after a step current is applied the cell currents will be similar. After a longer period of time the lower frequency response of the cells is excited and a greater difference in resistance is exhibited by each cell, causing the cell currents to diverge. When the magnitude of the applied current is larger, the self-balancing effect driven by the voltage difference is small relative to the cells' natural response to current excitation and the currents diverge. This means that aged cells within a parallel unit will see high currents like the newer cells, but only for a short period of time.

These effects can be observed in the experimental current data shown in Fig. 6. From 708 to 712 s, there are four increases in applied current magnitude, and each time the cell currents diverge after the step change. From 712 to 714 s there are two reductions in cell current and the cells self-balance following the voltage differences driven by the previously large currents. Note also the current response at 716—717 s where the applied current magnitude is quite low. In this case the convergent and divergent responses largely cancel each other out resulting in a consistent current over the 1 s period.

5.2. BEV application

Compared to a HEV, a BEV is more likely to operate in a much wider SOC window, and be subject to less dynamic loading. To consider this, a full discharge and CC-CV charge cycle is modelled, with charging and discharging currents both at 12 A (1C). For constant voltage charging, a means of translating cell voltage into applied current is required. Rather than creating a feedback system to control the input current, the current controller is assumed to be ideal in that it provides a current such that the cell is always at the requested voltage. In this instance, the applied current is calculated by rearranging the output of Eq. (17) to form (23), where v_{app} is the requested cell voltage. The peak current and charge throughput metrics are given in Table 5. The current fluctuations over the whole DOD mean that all of the cells experience a significantly higher peak current than if the cells were identical. In particular, cell 4, the most aged cell, sees over twice the nominal current at the end of the discharge. Despite this, the charge throughput results are more similar than for those recorded for the HEV case, because there is a greater opportunity for self-balancing during the load-cycle.

Table 4
HEV drive cycle simulation results for current and charge throughput.

Cell	Peak current (%)	Charge throughput (%)
1	114.4	28.6
2	99.5	25.1
3	101.1	25.5
4	91.5	21.9

Table 5
Discharge-charge drive cycle simulation results for current and charge throughput.

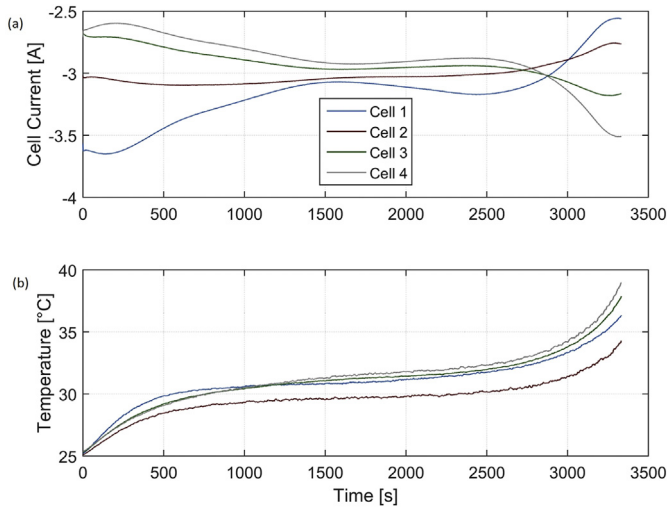| Cell	Peak current (%)	Charge throughput (%)
1	149.2	26.3
2	112.0	25.6
3	147.5	24.8
4	159.1	23.3

Fig. 7. Experimental cell currents (a) and temperatures (b) for a 1C discharge of aged cells connected in parallel.

$$i_1 = D'^{-1}\left(v_{app} - C'x\right) \tag{23}$$

While the current is lower magnitude and less dynamic than the HEV drive cycle, the wide SOC range gives greater opportunity for differences in v_{OC} and SOC. Fig. 7a shows the experimentally measured cell currents during a 1C discharge. There is a substantial change in current distribution after 2800 s, as the cells enter the low SOC region. By the end of discharge, the most aged cell (cell 4) is undergoing the largest current, and the least aged cell (cell 1) is undergoing the smallest current. This is at odds with the typically expected current distribution. This phenomenon has been previously reported in Refs. [13], where the authors attributed it to the increase in resistance that occurs at low SOCs. Less aged cells, which have previously undergone more current, will be at a lower SOC (although this in itself depends on their relative capacities) and so eventually their impedance will increase beyond the impedance of the more aged cells. This causes the more aged cells to see larger currents towards the end of the discharge. In addition to this, the V_{OC}s of some cell chemistries decreases more significantly at low SOCs. This means that during discharge the V_{OC} of lower SOC cells will be significantly closer to the terminal voltage and so less current is able to flow. Eq. (24) represents (1) re-arranged to solve for current, with RC pair voltages removed for simplicity. From this it can be seen that the resistance rise and lower v_{OC} both work to reduce the current through low SOC cells.

$$i_{cell} = \frac{v_t - v_{OC}}{R_D} \tag{24}$$

This all means that the performance of the cells is quite dynamic and varied and it is an oversimplification to assume that the current distribution is fixed and the most aged cell will always undergo the smallest current. The variation will be dependent on cell characteristics such as the v_{OC}-SOC curve and how the cell's impedance varies with SOC. Additionally, as highlighted here, the overall performance of the parallel cell unit will be application dependent and relate to the magnitude, duration and frequency content of the electrical load current. For example, a HEV battery pack is typically maintained within a narrow SOC window centred about 50% SOC. This means it won't undergo the same current switching discussed as a BEV may do.

The cell's temperature change during a discharge is known to be a function of impedance and current [28]. Fig. 7b shows the measured cell surface temperature corresponding to the discharge profile in Fig. 7a. The ambient temperature was regulated at 25 °C, and the temperatures were measured using T-type thermocouples attached to each cell, positioned midway along its length. At first, cell 1 undergoes the greatest temperature rise due to the respective large cell current. However, after 1000 s the temperature of cell 4 surpasses that of cell 1. By this point there is not as much difference in cell currents, and so the higher impedance of cell 4 causes greater heat generation despite the lower current. The temperature of cell 2 is consistently the lowest of all of the cells because it has a relatively low impedance without seeing the large currents experienced by cell 1.

5.3. Cell connections

A battery pack containing cells in parallel requires many cell interconnections to ensure all cells are in the current path. Typically, cells are grouped into parallel units, and each unit is then connected in series. Two potential issues relating to the connections within a parallel unit are considered: the connection resistance not being negligible, and the failure of a connection. Both of these have implications for the entire battery pack performance as well as for the current distribution within the parallel unit.

For the simulation results and verification of the modelling framework presented, it has been assumed that there is no additional resistance between each cell. For the experimental work, the wires from each cell were all connected to a common pair of terminals, so there was no unique connection between adjacent cells. However, often cells in parallel are connected in a 'ladder' format, such as that presented in Fig. 1b, in which the first cell is connected to the terminals, and the other cells are connected to each other. Ideally, the connection resistance (R_c in the Fig. 1b) would be zero, or at least negligible relative to cell impedance. However, if there is a poor connection it can have a significant impact on the pack as a whole [15]. The simulation study presented in Section 5.2 was repeated with R_c set to 5 mΩ, and the results are show in Table 6. The overall effect of this inclusion is to decrease the electrical load on the cells furthest from the terminals, as interconnection resistance accumulates. As a result, the charge throughput for cell 4 was a further 1% lower than in Section 5.2, but higher for the other cells. Similarly, the increased differences in effective impedance caused greater fluctuations in current, notably for three of the cells seeing higher peak currents. For the parallel system as a whole there was 1.34% less charge throughput, because the increased effective impedance of the parallel stack means that the minimum and maximum cell voltage limits are reached earlier when the cells are under electrical load.

If a cell disconnects from the parallel unit or malfunctions resulting in an internal open-circuit condition, which can occur through excessive vibration or shock loading [29], the remaining cells will continue to function. However, there will be a shorter discharge time because there is less total energy available and a greater effective parallel unit impedance that will further decrease energy availability and reduce power capability. This was simulated during a 1C discharge, where cell 2 was effectively disconnected

Table 6
Simulation results for current and charge throughput, with interconnection resistance.

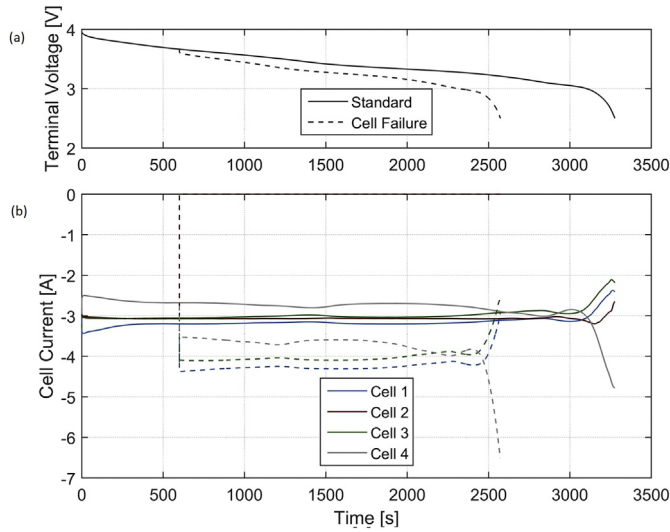| Cell	Peak current (%)	Charge throughput (%)
1	172.8	26.7
2	201.6	26.1
3	123.9	25.0
4	197.0	22.3

Fig. 8. Voltage (a) and cell current (b) for a simulated disconnect of cell 2 after 600 s.

after 600 s by setting its resistance to 10 kΩ. The results are summarised in Fig. 8, where solid lines represent the standard case, and the dashed lines represent the failure case. Fig. 8a shows the parallel unit terminal voltage, and Fig. 8b shows the four cell currents in both cases. There is an instantaneous drop in terminal voltage and increase in the magnitude of the remaining cell currents, and the parallel unit reaches the lower cut-off voltage 703 s earlier than if there had been no disconnection. In this case, there is a 55 mV drop in terminal voltage once the cell has disconnected, and an algorithm could be created to detect a sudden change in voltage without a corresponding change in current. However, if disconnection occurs under low, zero or a very dynamic load the disconnection may not be detected. The remaining cells, under load, are more likely to be taken outside of their intended window of operation for temperature and current.

6. Conclusions and future work

The primary results from the experimental and simulation work presented highlights that cells with different impedances and capacities connected in parallel do not behave in a uniform manner and can experience significantly different currents. The distribution of cell current is shown to be a complex function of impedance, including the high frequency aspects typically ignored for single cell models, and the difference in SOC between cells. As a conventional BMS design does not monitor current within parallel units, some cells may be taken above their intended operating current, or be aged more quickly due to increased charge throughput and ohmic heat generation − shortening the lifespan of the overall battery pack. Similarly, a cell losing electrical contact with the battery pack could result in poor SOC estimation, leading to the driver being misled about the available range of the vehicle.

A typical HEV drive cycle does not appear to cause a significant amount of SOC variation between cells in parallel due to its dynamic nature. However, for a BEV drive cycle that employs lower currents over a much larger DOD, cells can enter regions of nonlinearity. This causes significant variation and lead to cases where higher impedance cells can actually undergo larger currents. For both HEV and BEV applications, variations in current between different parallel connections of cells can cause uneven heat generation within a pack, which may require a higher degree of thermal management.

The new framework for parallel cell modelling and the validated instantiation of a simulation model for four 18650 cells connected electrically in parallel can be used to analyse the combined effect of cell-to-cell parameter variations and different usage profiles for both BEVs and HEVs applications. The same methodology may be further employed to simulate larger energy storage systems in which individual cell models are parameterised through a statistical process relative to a nominal cell to explore the impact that variations in cell characteristics, thermal and interconnection properties have on complete battery pack performance and expected life. Second-life applications are currently being explored, where cells at different SOHs are connected together for grid storage applications [30]. Using the parallel cell models developed here will allow for detailed simulations of the expected variations in current that may occur under load. This would further improve the design of the storage system and help ensure reliable operation. One considerable advantage of the proposed new model is that the parallel ECM is in the same form as a single cell model in which the causality between the terminal voltage and input current is maintained. This means that state observers and other control engineering techniques can now be developed for parallel units in the same way as they currently are for single cells or for cells connected electrically in series. This has the potential to make parallelized battery packs more reliable by improving fault detection methods. Another important aspect of cells in parallel is how they age. The results of this work show cells at a lower SOH typically see lower currents than other cells. This implies that they should age slower than the other cells, and so it is expected that gradually the SOHs of the cells within the parallel unit will converge. Ageing testing and analysis is currently being performed using the same cells to evaluate the impact of connecting cells in parallel on ageing and will be reported in a subsequent publication.

Nomenclature

Symbols

C	C rate of applied current (current scaled by capacity) h^{-1}
C_0	Effective charge capacitance of cell F
C_p	Polarisation capacitance of cell F
$i_{cell\,n}$	Cell current for cell n A
i_n	nth loop current in parallel cell mesh A
Q	Cell charge capacity Ah
R_c	Connection resistance between two parallel cells Ω
R_D	DC (ohmic) resistance of cell Ω
R_p	Polarisation resistance of cell Ω
SOC	State of charge of cell %
SOH	State of health of cell %
v_{app}	Applied terminal voltage during constant voltage charging V
v_{OC}	Open circuit voltage of cell V
v_p	Polarization voltage of cell V
v_t	Voltage at cell terminals V

References

[1] X. Gong, R. Xiong, C.C. Mi, Study of the characteristics of battery packs in electric vehicles with parallel-connected lithium-ion battery cells, in: Applied Power Electronics Conference and Exposition (APEC), 2014 Twenty-Ninth Annual IEEE, 2014, pp. 3218–3224, http://dx.doi.org/10.1109/APEC.2014.6803766.

[2] X. Zhang, C. Mi, Management of energy storage systems in EV, HEV and PHEV, Veh. Power Manag. (2011) 259–286, http://dx.doi.org/10.1007/978-0-85729-736-5_8. Springer London.

[3] U.D. of Energy, Advanced Vehicle Testing − Beginning-of-Test Battery Testing Results, 2011, pp. 1–5. http://www1.eere.energy.gov/vehiclesandfuels/avta/pdfs/fsev/battery_leaf_0356.pdf (accessed 10.22.14).

[4] J. Gallardo-Lozano, E. Romero-Cadaval, M.I. Milanes-Montero, M.A. Guerrero-Martinez, Battery equalization active methods, J. Power Sources 246 (2014) 934–949. http://dx.doi.org/10.1016/j.jpowsour.2013.08.026.

[5] Z. Zhang, P. Ramadass, Lithium-Ion battery systems and technology, in: R.J. Brodd (Ed.), Batteries for Sustainability, Springer, New York, 2013, pp. 319–357, http://dx.doi.org/10.1007/978-1-4614-5791-6_10.

[6] L. Zhong, C. Zhang, Y. He, Z. Chen, A method for the estimation of the battery pack state of charge based on in-pack cells uniformity analysis, Appl. Energy 113 (2014) 558–564. http://dx.doi.org/10.1016/j.apenergy.2013.08.008.

[7] L. Lu, X. Han, J. Li, J. Hua, M. Ouyang, A review on the key issues for lithium-ion battery management in electric vehicles, J. Power Sources 226 (2013) 272–288. http://dx.doi.org/10.1016/j.jpowsour.2012.10.060.

[8] A. Barré, B. Deguilhem, S. Grolleau, M. Gérard, F. Suard, D. Riu, A review on lithium-ion battery ageing mechanisms and estimations for automotive applications, J. Power Sources 241 (2013) 680–689. http://dx.doi.org/10.1016/j.jpowsour.2013.05.040.

[9] K. Maher, R. Yazami, A study of lithium ion batteries cycle aging by thermodynamics techniques, J. Power Sources 247 (2014) 527–533, http://dx.doi.org/10.1016/j.jpowsour.2013.08.053.

[10] B. Wu, V. Yufit, M. Marinescu, G.J. Offer, R.F. Martinez-Botas, N.P. Brandon, Coupled thermal−electrochemical modelling of uneven heat generation in lithium-ion battery packs, J. Power Sources 243 (2013) 544–554. http://dx.doi.org/10.1016/j.jpowsour.2013.05.164.

[11] K. Mueller, D. Tittel, L. Graube, Z. Sun, F. Luo, Optimizing BMS operating strategy based on precise SOH determination of lithium ion battery cells, in: Proceedings of the FISITA 2012 World Automotive Congress, Springer Berlin Heidelberg, 2013, pp. 807–819, http://dx.doi.org/10.1007/978-3-642-33741-3_9.

[12] X. Hu, J. Jiang, D. Cao, B. Egardt, Battery health prognosis for electric vehicles using sample entropy and sparse bayesian predictive modeling, Industrial Electron. IEEE Trans. PP (2015) 1, http://dx.doi.org/10.1109/TIE.2015.2461523.

[13] R. Gogoana, M.B. Pinson, M.Z. Bazant, S.E. Sarma, Internal resistance matching for parallel-connected lithium-ion cells and impacts on battery pack cycle life, J. Power Sources. 252 (2014) 8–13, http://dx.doi.org/10.1016/j.jpowsour.2013.11.101.

[14] L. Wang, Y. Cheng, X. Zhao, A LiFePO4 battery pack capacity estimation approach considering in-parallel cell safety in electric vehicles, Appl. Energy 142 (2015) 293–302, http://dx.doi.org/10.1016/j.apenergy.2014.12.081.

[15] G.J. Offer, V. Yufit, D.A. Howey, B. Wu, N.P. Brandon, Module design and fault diagnosis in electric vehicle batteries, J. Power Sources 206 (2012) 383–392. http://dx.doi.org/10.1016/j.jpowsour.2012.01.087.

[16] J. Kim, B.H. Cho, Screening process-based modeling of the multi-cell battery string in series and parallel connections for high accuracy state-of-charge estimation, Energy 57 (2013) 581–599. http://dx.doi.org/10.1016/j.energy.2013.04.050.

[17] T. Baumhöfer, M. Brühl, S. Rothgang, D.U. Sauer, Production caused variation in capacity aging trend and correlation to initial cell performance, J. Power Sources 247 (2014) 332–338. http://dx.doi.org/10.1016/j.jpowsour.2013.08.108.

[18] X. Hu, S. Li, H. Peng, A comparative study of equivalent circuit models for Li-ion batteries, J. Power Sources 198 (2012) 359–367, http://dx.doi.org/10.1016/j.jpowsour.2011.10.013.

[19] A. Seaman, T.-S. Dao, J. McPhee, A survey of mathematics-based equivalent-circuit and electrochemical battery models for hybrid and electric vehicle simulation, J. Power Sources 256 (2014) 410–423, http://dx.doi.org/10.1016/j.jpowsour.2014.01.057.

[20] A. Jossen, Fundamentals of battery dynamics, J. Power Sources 154 (2006) 530–538. http://dx.doi.org/10.1016/j.jpowsour.2005.10.041.

[21] M. Dubarry, N. Vuillaume, B.Y. Liaw, Origins and accommodation of cell variations in Li-ion battery pack modeling, Int. J. Energy Res. 34 (2010) 216–231, http://dx.doi.org/10.1002/er.1668.

[22] G.L. Plett, Extended Kalman filtering for battery management systems of LiPB-based HEV battery packs: part 2. Modeling and identification, J. Power Sources 134 (2004) 277–292. http://dx.doi.org/10.1016/j.jpowsour.2004.02.031.

[23] A. Farmann, W. Waag, A. Marongiu, D.U. Sauer, Critical review of on-board capacity estimation techniques for lithium-ion batteries in electric and hybrid electric vehicles, J. Power Sources 281 (2015) 114–130, http://dx.doi.org/10.1016/j.jpowsour.2015.01.129.

[24] W. Waag, S. Käbitz, D.U. Sauer, Experimental investigation of the lithium-ion battery impedance characteristic at various conditions and aging states and its influence on the application, Appl. Energy 102 (2013) 885–897. http://dx.doi.org/10.1016/j.apenergy.2012.09.030.

[25] D. Andre, M. Meiler, K. Steiner, C. Wimmer, T. Soczka-Guth, D.U. Sauer, Characterization of high-power lithium-ion batteries by electrochemical impedance spectroscopy. I. Experimental investigation, J. Power Sources 196 (2011) 5334–5341. http://dx.doi.org/10.1016/j.jpowsour.2010.12.102.

[26] N. Omar, M.A. Monem, Y. Firouz, J. Salminen, J. Smekens, O. Hegazy, et al., Lithium iron phosphate based battery − Assessment of the aging parameters and development of cycle life model, Appl. Energy 113 (2014) 1575–1585. http://dx.doi.org/10.1016/j.apenergy.2013.09.003.

[27] C. Fleischer, W. Waag, H.-M. Heyn, D.U. Sauer, On-line adaptive battery impedance parameter and state estimation considering physical principles in reduced order equivalent circuit battery models part 2 parameter and state estimation, J. Power Sources 262 (2014) 457–482, http://dx.doi.org/10.1016/j.jpowsour.2014.03.046.

[28] M. Debert, G. Colin, G. Bloch, Y. Chamaillard, An observer looks at the cell temperature in automotive battery packs, Control Eng. Pract. 21 (2013) 1035–1042. http://dx.doi.org/10.1016/j.conengprac.2013.03.001.

[29] M.A. Roscher, R.M. Kuhn, H. Döring, Error detection for PHEV, BEV and stationary battery systems, Control Eng. Pract. 21 (2013) 1481–1487. http://dx.doi.org/10.1016/j.conengprac.2013.07.003.

[30] P. Cicconi, D. Landi, A. Morbidoni, M. Germani, Feasibility analysis of second life applications for Li-Ion cells used in electric powertrain using environmental indicators, in: Energy Conference and Exhibition (ENERGYCON), 2012 IEEE International, 2012, pp. 985–990, http://dx.doi.org/10.1109/EnergyCon.2012.6348293.